Properties of Cosmic Lithium Isotopes Measured by the Alpha Magnetic Spectrometer SUPPLEMENTAL MATERIAL

For references see the main text.

Detector.—AMS is a general purpose high-energy particle physics detector in space. The layout of the detector is shown in Fig. S1. The main elements are the permanent magnet, the silicon tracker, four planes of time of flight (TOF) scintillation counters, the array of anticoincidence counters (ACCs), a transition radiation detector (TRD), a ring imaging Čerenkov detector (RICH), and an electromagnetic calorimeter (ECAL).

The AMS coordinate system is concentric with the magnet. The x axis is parallel to the main component of the magnetic field and the z axis points vertically with $z = 0$ at the center of the magnet. The (y-z) plane is the bending plane. Above, below, and downward-going refer to the AMS coordinate system. The central field of the magnet is 1.4 kG. Before flight, the field was measured in 120 000 locations to an accuracy of better than 2 G. On orbit, the magnet temperature varies from -3 to $+20$°C. The field strength is corrected with a measured temperature dependence of $-0.09\%/$°C.

The tracker has nine layers, the first ($L1$) at the top of the detector, the second ($L2$) just above the magnet, six ($L3$ to $L8$) within the bore of the magnet, and the last ($L9$) just above the ECAL. $L2$ to $L8$ constitute the inner tracker. Each layer contains double-sided silicon microstrip detectors that independently measure the x and y coordinates. The tracker accurately determines the trajectory of cosmic rays by multiple measurements of the coordinates with a resolution in each layer of 5.8 μm for Li nuclei in the bending (y) direction. Together, the tracker and the magnet measure the rigidity of charged cosmic rays.

Each layer of the tracker provides an independent measurement of the charge number Z with a resolution of $\sigma_Z/Z = 5.6\%$ for $Z = 3$ particles. Overall, the inner tracker has a resolution of $\sigma_Z/Z = 2.5\%$ for $Z = 3$ particles.

Two TOF planes are located above the magnet (upper TOF) and two planes are below the magnet (lower TOF). The overall velocity ($\beta = v/c$) resolution has been measured to be $\sigma(1/\beta) = 0.015$ for Z=3 particles. The pulse heights of the two upper planes are combined to provide an independent measurement of the charge with an accuracy $\sigma_Z/Z = 3.5\%$ for Z=3 particles. The pulse heights from the two lower planes are combined to provide another independent charge measurement with the same accuracy.

The RICH detector [30] measures the particle velocity and charge magnitude. It is located below the lower TOF and consists of two radiators, an expansion volume, and a photo-detection plane. The dielectric radiators induce the emission of a cone of Čerenkov photons when traversed by charged particles with a velocity greater than the velocity of light in the radiator. The central radiator is formed by sodium fluoride (RICH-NaF) of refractive index $n = 1.33$, it is surrounded by silica aerogel (RICH-Agl) of refractive index $n = 1.05$. This allows the detection of particles with velocities $\beta > 0.75$ for those that pass through the NaF radiator and $\beta > 0.952$ for those that pass through the Agl radiator. The expansion volume extends along z for 470 mm between the radiators and the photo-detection plane and it is surrounded by a high reflectivity mirror to increase detection efficiency. The photo-detection plane is an array of 10880 photosensors in multi-channel photomultiplier tubes with an effective spatial granularity of 8.5×8.5 mm^2. For $Z = 3$ particles, the RICH velocity resolution, σ_β, is 1.8×10^{-3} for NaF and 5.5×10^{-4} for Agl at $\beta \simeq 1$.

Li nuclei traversing AMS were triggered as described in Ref. [31]. The trigger efficiency has been measured to be >99% over the entire rigidity range.

Monte Carlo simulated events were produced using a dedicated program developed by the collaboration based on the GEANT4-10.3 package [32]. The program simulates electromagnetic and hadronic interactions of particles in the material of AMS and generates

detector responses. The digitization of the signals is simulated precisely according to the measured characteristics of the electronics. The simulated events then undergo the same reconstruction as used for the data.

Event selection.— The collection time used in this analysis includes only those time periods during which the detector was in normal operating conditions and, in addition, AMS was pointing within 40° of the local zenith, and the International Space Station (ISS) was outside of the South Atlantic Anomaly. Because of the influence of the geomagnetic field, the collection time for Galactic cosmic rays increases with rigidity, reaching 2.6×10^8 seconds at 25 GV.

Li nuclei are required to be downward going and to have a reconstructed track in the inner tracker which passes through $L1$. Charge measurements on $L1$, the upper TOF, the inner tracker, and the lower TOF are required to be compatible with $Z = 3$. Track fitting quality criteria such as a χ^2/d.o.f. < 10 in the bending plane are applied. To reduce the background from heavier nuclei interacting in the AMS materials above tracker $L2$, events having secondary tracks with rigidity > 0.5 GV are removed.

To ensure an accurate velocity measurement by the TOF, additional quality criteria, such as consistency of time measurements from the four TOF layers, are applied.

For events with a velocity above the Čerenkov thresholds, additional quality criteria, such as the number of photomultiplier tubes in the reconstructed Čerenkov ring ≥ 3, the number of photoelectrons in the reconstructed Čerenkov ring $\geq$20% of the total number of photoelectrons, the charge measured by RICH $Z_{\rm RICH} > 2$, and compatible velocity measurements in TOF and RICH, are required.

The measured rigidity is required to be greater than a factor of 1.2 times the maximum geomagnetic cutoff within the AMS field of view. The cutoff at each ISS location was calculated by backtracing from the top of AMS out to 50 Earth's radii using the most recent International Geomagnetic Reference Field model [33].

Background estimation.— Because of the multiple independent measurements of the charge, the charge confusion from noninteracted nuclei is negligible (<0.01%) over the entire rigidity range. The residual background comes from heavier nuclei which interact above tracker $L2$.

The background resulting from interactions in the material between $L1$ and $L2$ (TRD and upper TOF) is evaluated by fitting the charge distribution of tracker $L1$ with charge distribution templates of Li, Be, B, and C. Then cuts are applied on the $L1$ charge as shown in Fig. S2. This background is found to be negligible (<0.1%) over the entire rigidity range.

The background from interactions in materials above $L1$ (thin support structures made by carbon fiber and aluminum honeycomb) has been estimated from simulation using MC samples generated according to AMS flux measurements [9]. The simulation of nuclear interactions has been validated using data [8]. The main contribution to this background comes from carbon nuclei. The isotopic composition of the background from carbon nuclei fragmenting to lithium is evaluated using events with measured $Z = 6$ in tracker $L1$ and $Z = 3$ in the inner tracker ($L2$-$L8$). Identification of lithium isotopes has been performed using the fitting procedure described below. Figure S3 shows the measured branching ratio: C $\rightarrow$ ^{6}Li/C $\rightarrow$ Li, together with the MC simulation. As seen, the MC simulation and data are in good agreement below 5 GeV/n. Above 5 GeV/n, the small difference between data and MC was taken into account while calculating the background uncertainty. The total background was found to be 1.0% for ^{6}Li and 1.1% for ^{7}Li at 2 GV, decreasing to 0.2% at 10 GV and 0.1% at 25 GV for both ^{6}Li and ^{7}Li. The contribution from C cosmic rays amounts

to 50% of the background, followed by O cosmic rays with a 20% contribution. Other heavy cosmic nuclei ranging from Be to Fe contribute a total of 30%. The uncertainties on the fluxes due to background were evaluated to be 0.4% at 2 GV, decreasing to 0.1% at 10 GV and 0.05% at 25 GV.

The additional background to ^{6}Li from the fragmentation of $^7\mathrm{Li} \rightarrow {}^6\mathrm{Li}$ within the AMS materials is estimated from the MC simulation to be <1.8% in the entire rigidity range. The uncertainty on the ^{6}Li flux due to this background was evaluated to be <0.9% in the entire rigidity range.

After background subtraction we obtain 0.97 million ^{6}Li and 1.04 million ^{7}Li nuclei.

Fitting procedure.— The number of events N_i^{A} in the ith rigidity bin $(R_i, R_i + \Delta R_i)$, see Eq. (1), for the two isotopes ^{6}Li (A = 6) and ^{7}Li (A = 7) are obtained by fitting the measured inverse mass distribution 1/M with ^{6}Li and ^{7}Li inverse mass templates. The mass M is determined by combining the rigidity R measured by the tracker with the velocity β measured by the TOF, the RICH-NaF, or the RICH-Agl, as follows:

$$M = \frac{R \cdot Ze}{\beta\gamma}, \tag{S1}$$

where the charge number Z is 3 for lithium nuclei, and $\gamma = 1/\sqrt{1-\beta^2}$ is the Lorentz factor. The corresponding mass uncertainty ΔM is defined by the relation $\Delta M/M = \sqrt{(\sigma_R/R)^2 + \gamma^4(\sigma_\beta/\beta)^2}$, where σ_R is the rigidity resolution and σ_β is the velocity resolution. The γ^4 term in the above relation leads to the deterioration in the isotope mass separation at high rigidities, and consequently prevents the measurement of the corresponding isotope fluxes. With the velocity resolution for the AMS RICH-Agl $\sigma_\beta = 5.5 \times 10^{-4}$, the highest rigidity is chosen to be 25 GV to obtain an accurate measurement of Li isotope fluxes.

To reduce the bin to bin migration corrections and ensure that the same detector among TOF, RICH-NaF, and RICH-Agl is used for the velocity measurement for both lithium isotopes, the N_i^{A} were computed by fitting the inverse mass distribution in the kinetic energy per nucleon E_K space, where $E_K \equiv (\gamma - 1) \cdot (\mathrm{M}^{^6\mathrm{Li}} + \mathrm{M}^{^7\mathrm{Li}})/13$, and $\mathrm{M}^{^6\mathrm{Li}}$ and $\mathrm{M}^{^7\mathrm{Li}}$ are the ^{6}Li and ^{7}Li masses. To have both isotope flux measurements in the same rigidity bins, a procedure consisting of transforming the 28 rigidity bins into two sets of 28 kinetic energy per nucleon bins corresponding to ^{6}Li and ^{7}Li, respectively, and fitting the inverse mass in each of these two sets of E_K bins was applied. This fitting procedure is detailed below.

First, a set of 28 E_K bins were constructed from the rigidity bins using

$$(E_K^i, E_K^i + \Delta E_K^i) = \left(\sqrt{\left(\frac{R_i Ze}{\mathrm{A}}\right)^2 + \left(\frac{\mathrm{M}}{\mathrm{A}}\right)^2} - \frac{\mathrm{M}}{\mathrm{A}}, \sqrt{\left(\frac{(R_i + \Delta R_i)Ze}{\mathrm{A}}\right)^2 + \left(\frac{\mathrm{M}}{\mathrm{A}}\right)^2} - \frac{\mathrm{M}}{\mathrm{A}} \right), \tag{S2}$$

with charge number $Z = 3$, atomic mass number A = 6 and mass $\mathrm{M} = \mathrm{M}^{^6\mathrm{Li}}$. Then, the $N_{i=1\ldots28}^{\mathrm{A}=6}$ event numbers were obtained by fitting the inverse mass distributions in these E_K bins with ^{6}Li and ^{7}Li inverse mass templates. Examples of the results from this step of the fitting procedure are shown in Fig. S4.

Next, another set of 28 E_K bins was constructed from the same rigidity bins using Eq. (S2), but with atomic mass number A = 7 and mass $\mathrm{M} = \mathrm{M}^{^7\mathrm{Li}}$. The $N_{i=1\ldots28}^{\mathrm{A}=7}$ event numbers were obtained by fitting the inverse mass distributions with ^{6}Li and ^{7}Li inverse mass templates in these E_K bins. Examples of the results from this step of the fitting procedure are shown in Fig. S5.

The ^{6}Li and ^{7}Li inverse mass templates have been obtained from the MC simulation using rigidity and velocity resolution functions, described below.

Rigidity and velocity resolution functions.— The rigidity resolution function, determined from MC simulations, has been extensively verified with the data [8]. The velocity resolution functions of TOF and RICH are determined from the MC simulation and have been verified with the data, see Fig. S6. To verify the rigidity and velocity resolution functions simultaneously, the distribution of the ^{7}Li inverse mass was obtained from the data using the geomagnetic cutoff as a filter. When ^{6}Li and ^{7}Li nuclei with a specific E_K encounter the Earth's magnetic field, only ^{7}Li, with its higher rigidity compared to ^{6}Li, is able to reach the AMS detector. With this method we obtained ^{7}Li inverse mass distributions in three rigidity bins in the TOF, RICH-NaF, and RICH-Agl velocity measurement ranges and we compared them to the corresponding distributions from MC simulation, as shown in Fig. S7. As seen, the MC simulation agrees well with data.

Uncertainties related to the rigidity and velocity resolution functions have been studied extensively. For the rigidity resolution functions, the uncertainty was obtained by independently varying the width of the Gaussian core of the rigidity resolution functions by 5%, as well as the amplitude of the non-Gaussian tails of these resolution functions by 10% [8]. The corresponding systematic error on the fluxes due to the rigidity resolution functions is <0.8% over the entire rigidity range.

For the velocity resolution functions of the TOF, the uncertainty arises from limitations in the TOF calibration accuracy due to details in photon propagation in the TOF scintillators and light guides. Before launch, at the CERN SPS, AMS was extensively calibrated with 180 and 400 GeV/c proton beams and beams of positrons, electrons, and pions from 10 to 290 GeV/c. In total, calibrations with 18 different energies and particles at 2000 positions, including from the top to the bottom and from bottom to top of the AMS, were performed. These data allow the TOF calibration at $\beta = -1$ (upward-going particles in the AMS coordinate system), and $\beta = +1$ (downward-going particles) and therefore the determination of the uncertainty of the TOF velocity scale. The uncertainty of the TOF velocity scale was additionally verified using He nuclei with rigidities above 30 GV collected with the AMS horizontal, that is, when the ISS was oriented such that the AMS was pointing within $90^\circ \pm 10^\circ$ of the local zenith. In this condition, high rigidity He nuclei can travel from the top to the bottom and from bottom to the top. Figure S8 shows the ratio of rigidity-derived velocity $\beta_{\rm Tracker}$ and TOF measured velocity $\beta_{\rm TOF}$ for He nuclei with rigidities above 30 GV for (a) downward and (b) upward directions. As seen, the uncertainty of the TOF velocity scale is $10^{-3} \times (1 - \beta)$. The corresponding systematic error on the fluxes due to the TOF velocity resolution function uncertainties is <1.7% below 4 GV.

For the velocity resolution functions of the RICH-NaF and the RICH-Agl, the uncertainties of the RICH velocity scale are due to the accuracy of the measurement of the expansion volume extent D (∼1.4 mm). This measurement was done during the AMS construction and verified in flight by measurements of the reconstructed RICH ellipse parameters on the photo-detection plane with high rigidity nuclei passing through the NaF radiator, where the refractive index is known to high accuracy ($n_{\rm NaF}$= 1.3253 at 600 nm) and using the relation $\mathrm{D} = r \cdot \sqrt{2 - n_{\rm NaF}^2}/\sqrt{n_{\rm NaF}^2 - 1}$, where r is the semi-minor axis of the RICH ellipse. The uncertainty in the value of the expansion volume extent D was additionally verified using high statistics He events, using the method described in Ref. [35], see in particular Fig. S2 from Ref. [35]. Figure S9 shows the difference between data and MC simulation for the reconstructed RICH velocity $\beta_{\rm RICH}$ using ^{4}He events as a function of rigidity-derived velocity $\beta_{\rm Tracker}$ for (a) the RICH-NaF radiator and (b) the RICH-Agl radiator. The solid red lines show the estimated difference between data and the MC simulation due to the uncertainty in

the expansion volume extent D. As seen, all the measured points are within the systematic uncertainty. The corresponding systematic error on the fluxes due to the RICH velocity resolution functions is <1.3% above 4 GV.

Further studies on the $\Phi^{^7\mathrm{Li}}/\Phi^{^6\mathrm{Li}}$ rigidity dependence.— To verify the important observation made with Eq. (4), we fit $\Phi^{^7\mathrm{Li}}/\Phi^{^6\mathrm{Li}}$ over the entire rigidity range with a double power law

$$\Phi^{^7\mathrm{Li}}/\Phi^{^6\mathrm{Li}} = \begin{cases} K\,(R/R_0)^{\Delta_1}, & R \le R_0, \\ K\,(R/R_0)^{\Delta_2}, & R > R_0. \end{cases} \tag{S3}$$

The result is shown in Fig. S14. The fit yields $K = 1.17 \pm 0.02$, $R_0 = 7.2 \pm 0.4$ GV, $\Delta_1 = 0.21 \pm 0.01$, and $\Delta_2 = -0.002 \pm 0.011$ with a χ^2/d.o.f. of 23.8/24. The value of Δ_2 is consistent with zero, which further confirms that $\Phi^{^6\mathrm{Li}}$ and $\Phi^{^7\mathrm{Li}}$ have an identical rigidity dependence above $R_0 \sim 7$ GV.

Estimation of primary ^{7}Li flux fraction.— Using the AMS O flux [46], Φ^{O}, as an estimator of the primary ^{7}Li flux rigidity dependence $\Phi^{^7\mathrm{Li}}_{\mathrm{primary}} = f_{\mathrm{O}} \times \Phi^{\mathrm{O}}$ and the AMS ^{6}Li flux rigidity dependence $\Phi^{^6\mathrm{Li}}$ for the secondary ^{7}Li flux rigidity dependence $\Phi^{^7\mathrm{Li}}_{\mathrm{secondary}} = c \times \Phi^{^6\mathrm{Li}}$, with $\Phi^{^7\mathrm{Li}} = \Phi^{^7\mathrm{Li}}_{\mathrm{primary}} + \Phi^{^7\mathrm{Li}}_{\mathrm{secondary}}$, we fit the AMS ^{7}Li/^{6}Li flux ratio above 7 GV with

$$\frac{\Phi^{^7\mathrm{Li}}}{\Phi^{^6\mathrm{Li}}} = c + \frac{f_{\mathrm{O}} \times \Phi^{\mathrm{O}}}{\Phi^{^6\mathrm{Li}}}. \tag{S4}$$

The fit yields $c = 1.17^{+0.02}_{-0.03}$ and $f_{\mathrm{O}} = 0^{+2.7\times10^{-3}}_{-0}$ with a χ^2/d.o.f. of 12/13, see Fig. S15. This corresponds to a fraction of the primary ^{7}Li flux of <3% at the 90% C.L.

Alternatively, we have used the AMS ^{4}He flux, $\Phi^{^4\mathrm{He}}$, as the primary ^{7}Li flux rigidity dependence estimator, $\Phi^{^7\mathrm{Li}}_{\mathrm{primary}} = f_{^4\mathrm{He}} \times \Phi^{^4\mathrm{He}}$ and the AMS ^{6}Li flux rigidity dependence $\Phi^{^6\mathrm{Li}}$ for the secondary ^{7}Li flux rigidity dependence, $\Phi^{^7\mathrm{Li}}_{\mathrm{secondary}} = c \times \Phi^{^6\mathrm{Li}}$. The $\Phi^{^4\mathrm{He}}$ was obtained from the AMS time-averaged He flux from Ref. [39], Φ^{He} and the fit in Ref. [41], $\Phi^{^3\mathrm{He}}/\Phi^{^4\mathrm{He}} = 0.142(R/4.5\,\mathrm{GV})^{-0.289}$, with $\Phi^{\mathrm{He}} = \Phi^{^3\mathrm{He}} + \Phi^{^4\mathrm{He}}$ and

$$\Phi^{^4\mathrm{He}}(R) = \frac{\Phi^{\mathrm{He}}}{1 + \Phi^{^3\mathrm{He}}/\Phi^{^4\mathrm{He}}} = \frac{\Phi^{\mathrm{He}}}{1 + 0.142(R/4.5\ \mathrm{GV})^{-0.289}}.$$

We fit the AMS ^{7}Li/^{6}Li flux ratio above 7 GV with

$$\frac{\Phi^{^7\mathrm{Li}}}{\Phi^{^6\mathrm{Li}}} = c + \frac{f_{^4\mathrm{He}} \times \Phi^{^4\mathrm{He}}}{\Phi^{^6\mathrm{Li}}}. \tag{S5}$$

The fit yields $c = 1.17^{+0.02}_{-0.04}$ and $f_{^4\mathrm{He}} = 0^{+1.3\times10^{-4}}_{-0}$ with a χ^2/d.o.f. of 12/13. This corresponds to a fraction of the primary ^{7}Li flux of <5% at the 90% C.L.

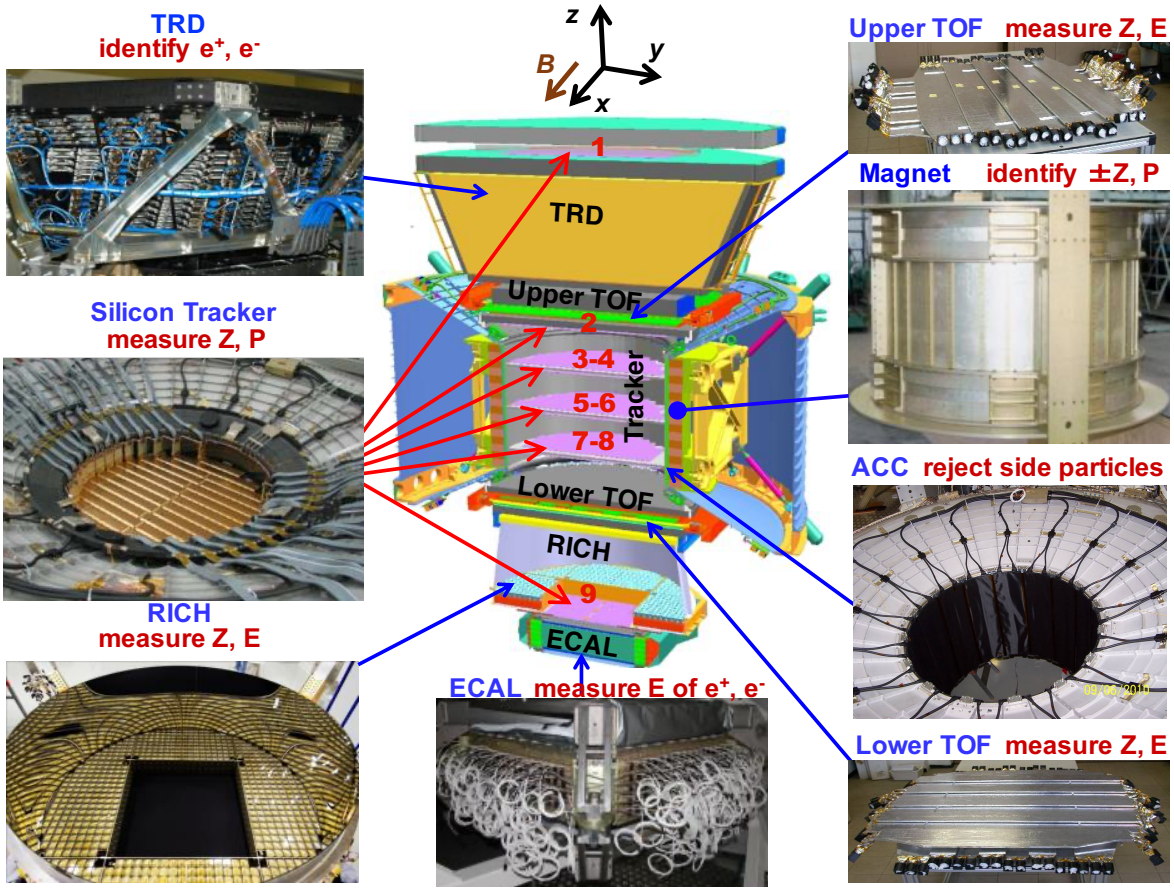

FIG. S1. The AMS detector, its main components and their functions. AMS is a TeV precision, multipurpose particle physics magnetic spectrometer in space. It identifies particles and nuclei by their charge number Z, energy E, and momentum P or rigidity ($R = Pc/Ze$), which are derived from redundant measurements by combinations of the Tracker, TOF, RICH, and ECAL. The ACC counters, located in the magnet bore, are used to reject particles entering AMS from the side. The AMS coordinate system is also shown. The x axis is parallel to the main component of the magnetic field and the z axis points vertically with $z = 0$ at the center of the magnet.

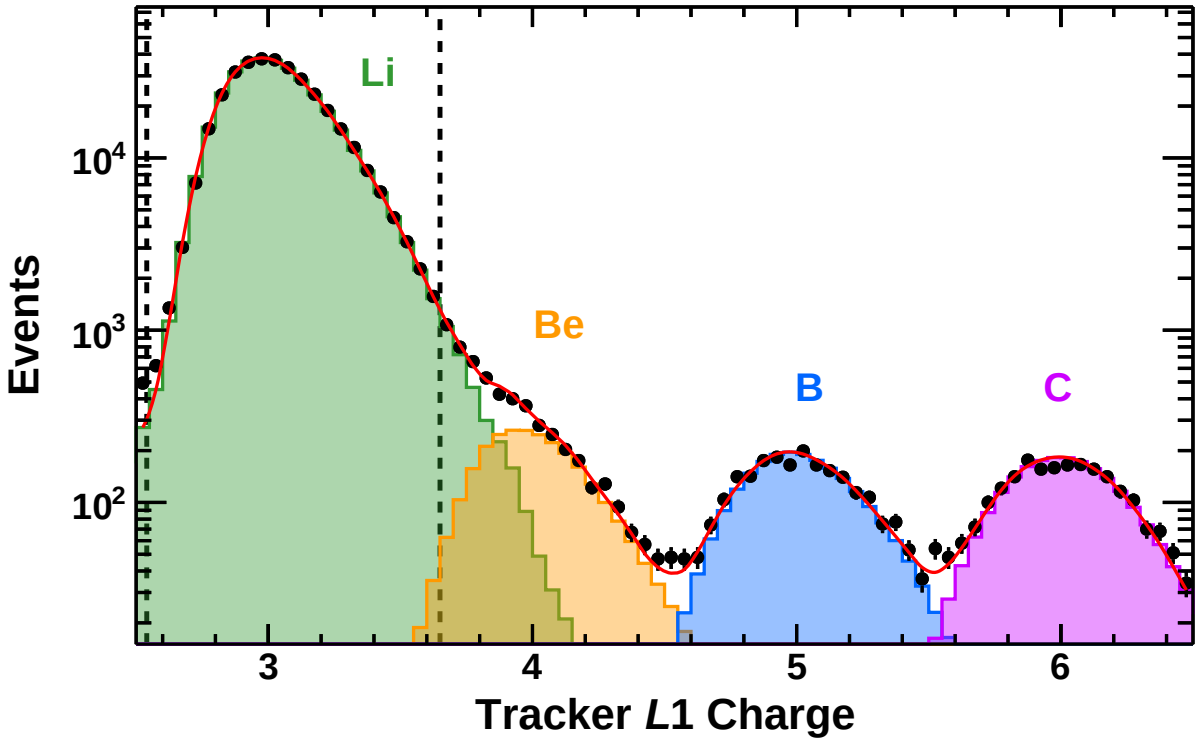

FIG. S2. Charge distribution measured by tracker $L1$ for lithium (^{6}Li+^{7}Li) events selected by the inner tracker in the 0.9−1.2 GeV/n kinetic energy range (black points). The solid red curve shows the fit of the sum of the charge distribution templates for Li (green), Be (orange), B (light blue), and C (violet) to the data. The templates are obtained from a selection of non-interacting samples on $L2$ by the use of the charge measurement from $L1$ and $L3$-$L8$. The charge selection cuts applied on $L1$ are shown as vertical dashed lines.

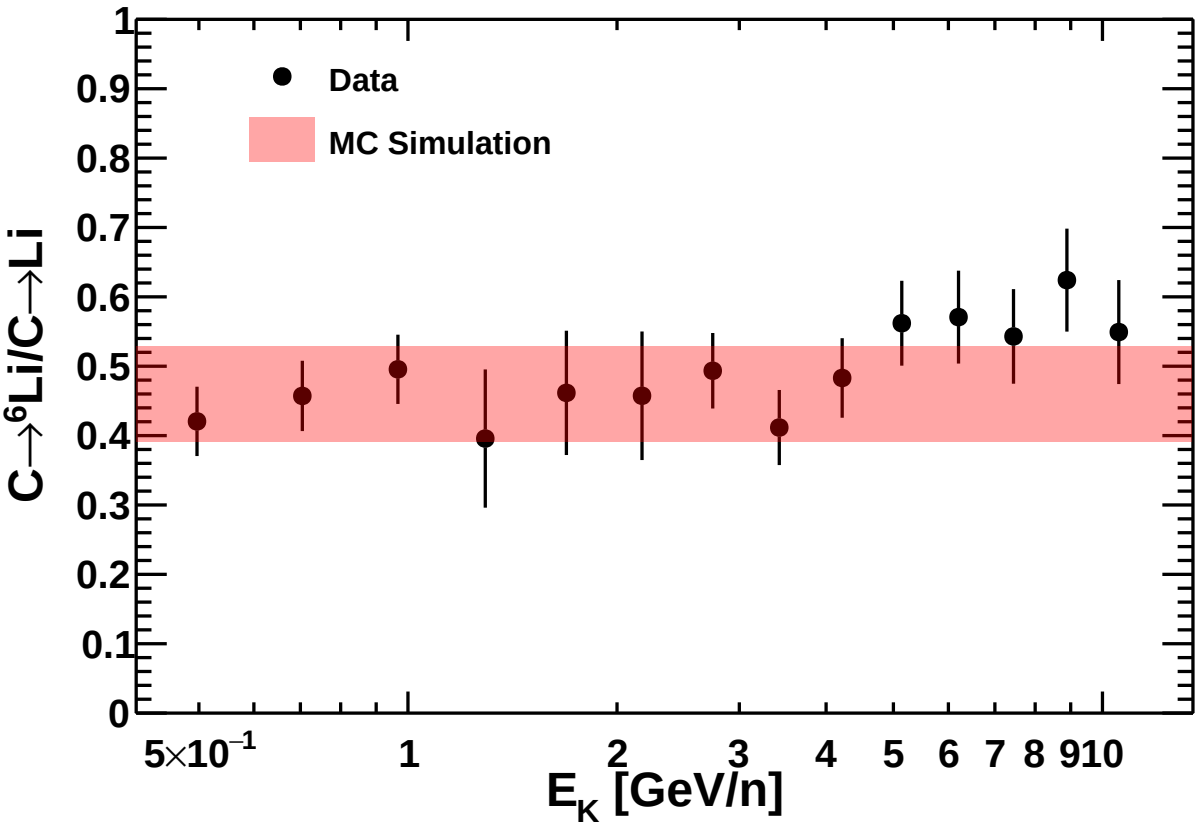

FIG. S3. Branching ratio of carbon nuclei fragmenting to ^{6}Li: C $\rightarrow$ ^{6}Li/C $\rightarrow$ Li, due to interactions in the AMS material between tracker $L1$ and $L2$, estimated from data (black points) and from MC simulation (red band, $\sim$15% uncertainty). As seen, the MC simulation and data are in good agreement below 5 GeV/n. Above 5 GeV/n, the small difference between data and MC was taken into account while calculating the background uncertainty.

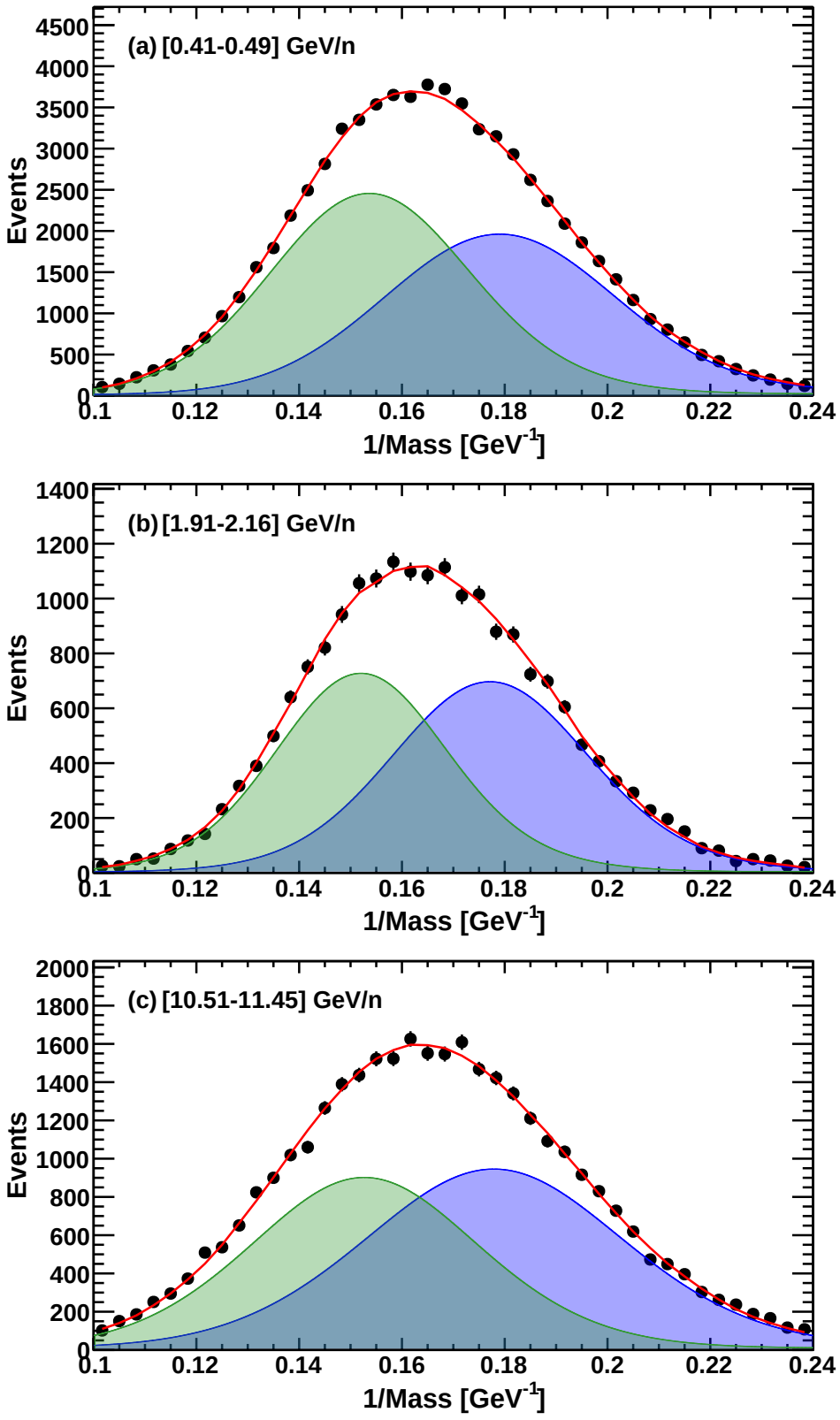

FIG. S4. Inverse mass distributions for ^{6}Li+^{7}Li data (black points) for three E_K bins selected using (a) the TOF [0.41-0.49] GeV/n, (b) the RICH-NaF [1.91-2.16] GeV/n, and (c) the RICH-Agl [10.51-11.45] GeV/n. These three E_K bins correspond to ^{6}Li rigidity bins of [1.92-2.15] GV, [5.37-5.90] GV, and [22.8-24.7] GV, respectively. The red curves show the fits of the sum of the ^{6}Li (blue) and ^{7}Li (green) MC templates to the data with χ^2/d.o.f. = (a) 33/40, (b) 33/40, and (c) 22/40.

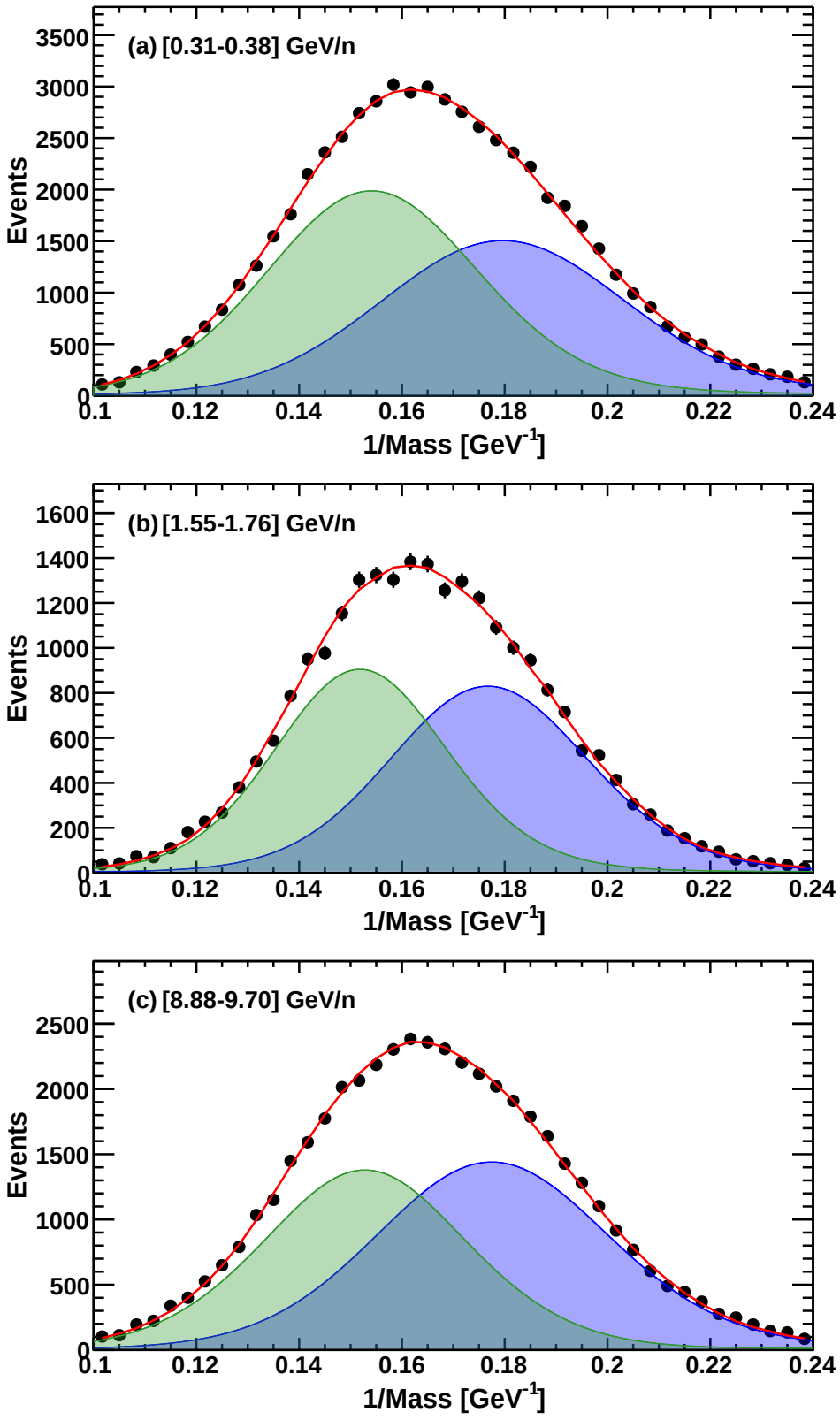

FIG. S5. Inverse mass distributions for ^{6}Li+^{7}Li data (black points) for three E_K bins selected using (a) the TOF [0.31-0.38] GeV/n, (b) the RICH-NaF [1.55-1.76] GeV/n, and (c) the RICH-Agl [8.88-9.70] GeV/n. These three E_K bins correspond to ^{7}Li rigidity bins of [1.92-2.15] GV, [5.37-5.90] GV, and [22.8-24.7] GV, respectively. The red curves show the fits of the sum of the ^{6}Li (blue) and ^{7}Li (green) MC templates to the data with χ^2/d.o.f. = (a) 38/40, (b) 40/40, and (c) 20/40.

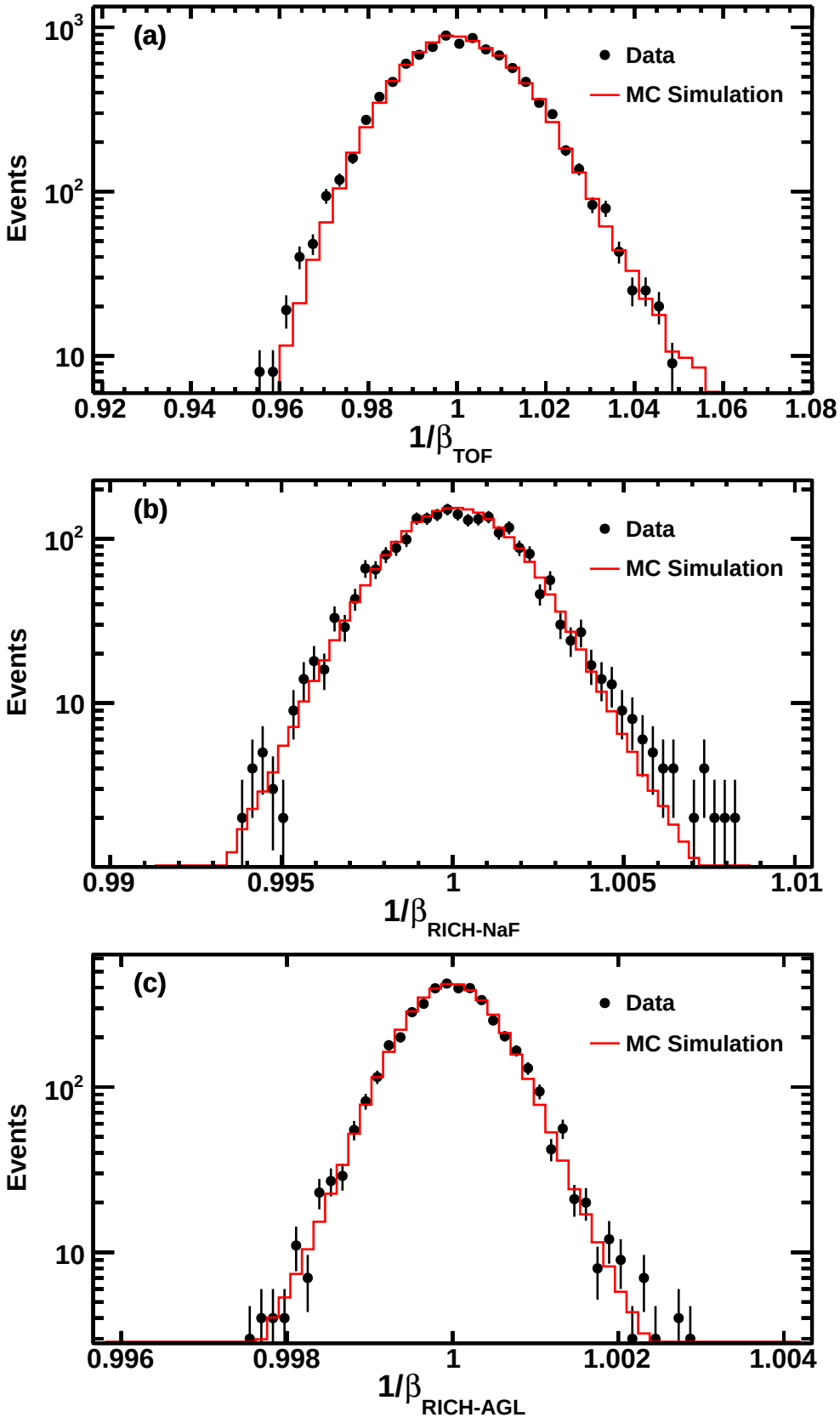

FIG. S6. Comparison between ^{6}Li+^{7}Li data (black points) and MC simulation (red histogram) of the inverse velocity ($1/\beta$) distributions at $\beta \simeq 1$, obtained using (a) the TOF, (b) the RICH-NaF, and (c) the RICH-Agl. Events are selected with R >100 GV for (a) and (b), and with R >200 GV for (c). As seen, the MC simulation agrees well with the data.

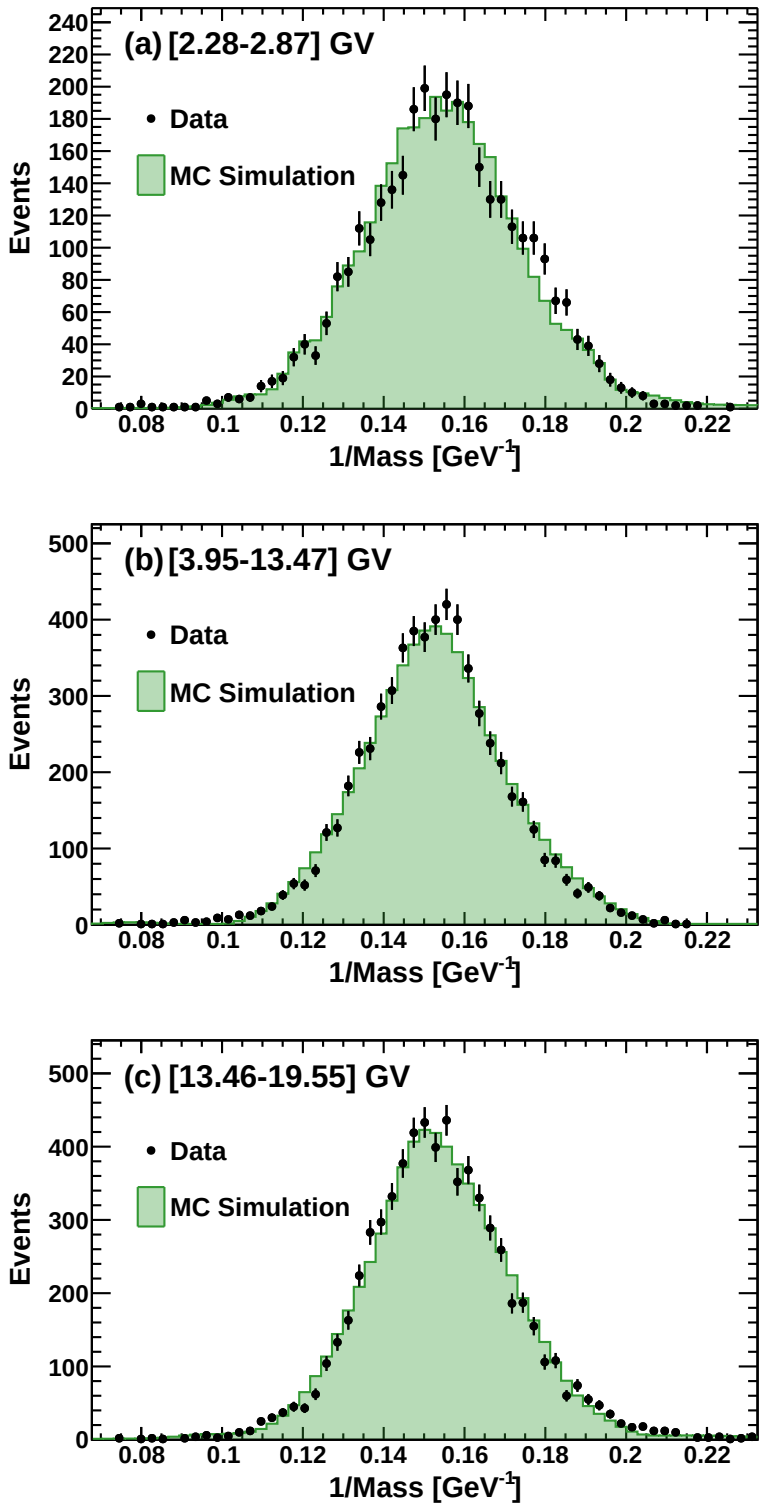

FIG. S7. Comparison of the ^{7}Li inverse mass distributions from data (black dots) and from MC simulation (green histogram) obtained using the geomagnetic cutoff as a filter, for three rigidity bins selected using (a) the TOF, (b) the RICH-NaF, and (c) the RICH-Agl. As seen, the MC simulation agrees well with the data.

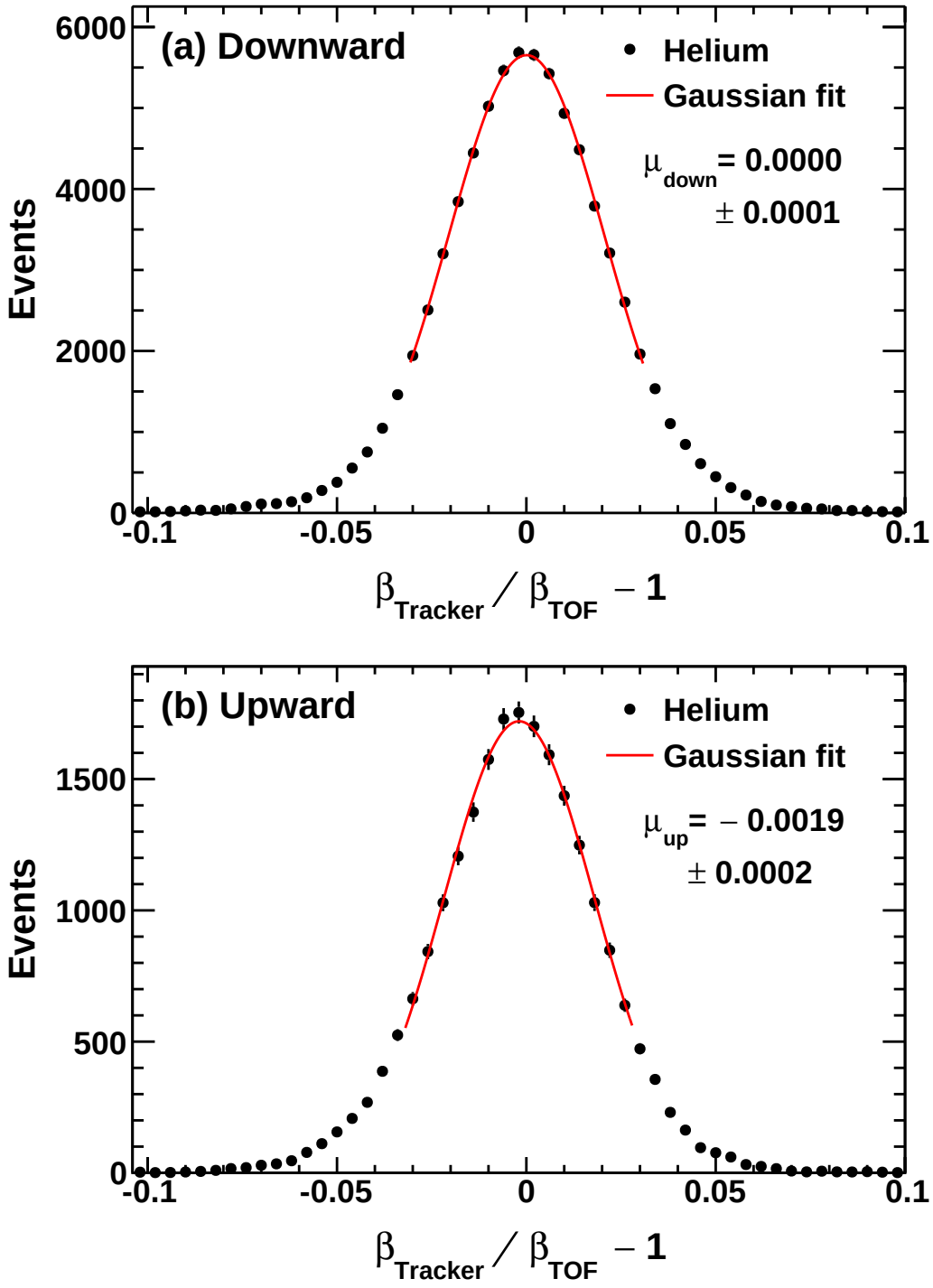

FIG. S8. The ratio of rigidity-derived velocity $\beta_{\rm Tracker} = 2R/\sqrt{4R^2 + {\rm M}_{\rm He}^2}$, where $\rm M_{He}$ is the average helium mass estimated based on the helium isotope composition from Ref. [41], and the TOF velocity $\beta_{\rm TOF}$ for He nuclei with rigidities above 30 GV for (a) downward and (b) upward directions. The red curves show results of the Gaussian fit with means of $\mu_{\rm down} = 0.0000 \pm 0.0001$ and $\mu_{\rm up} = -0.0019 \pm 0.0002$ for downward and upward directions, respectively. As seen, the maximum uncertainty of the TOF velocity scale is $|\mu_{\rm down} + \mu_{\rm up}|/2 = 10^{-3}$, which corresponds to an uncertainty in the z positions of the upper TOF and lower TOF of 1 mm.

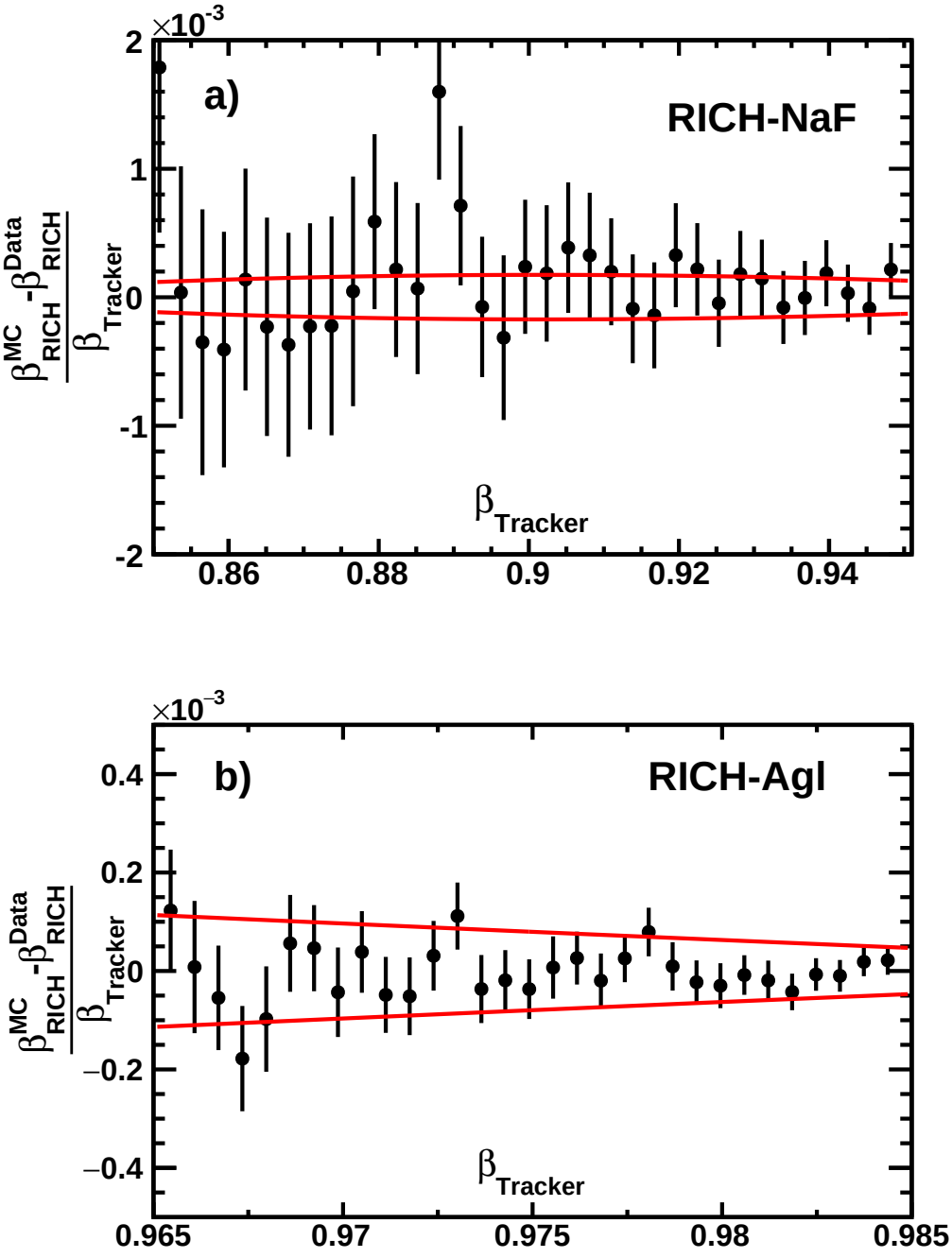

FIG. S9. The difference between data and the MC simulation for the reconstructed RICH velocity β_{RICH} using ^{4}He events as a function of rigidity R measured by the inner tracker, converted to velocity as $\beta_{\mathrm{Tracker}} = 2R/\sqrt{4R^2 + \mathrm{M}^2_{^4\mathrm{He}}}$ for (a) the RICH-NaF radiator and (b) the RICH-Agl radiator. The solid red lines show the estimated difference between data and MC simulation due to the uncertainty in the expansion volume extent D. As seen, all the measured points are within the systematic uncertainty.

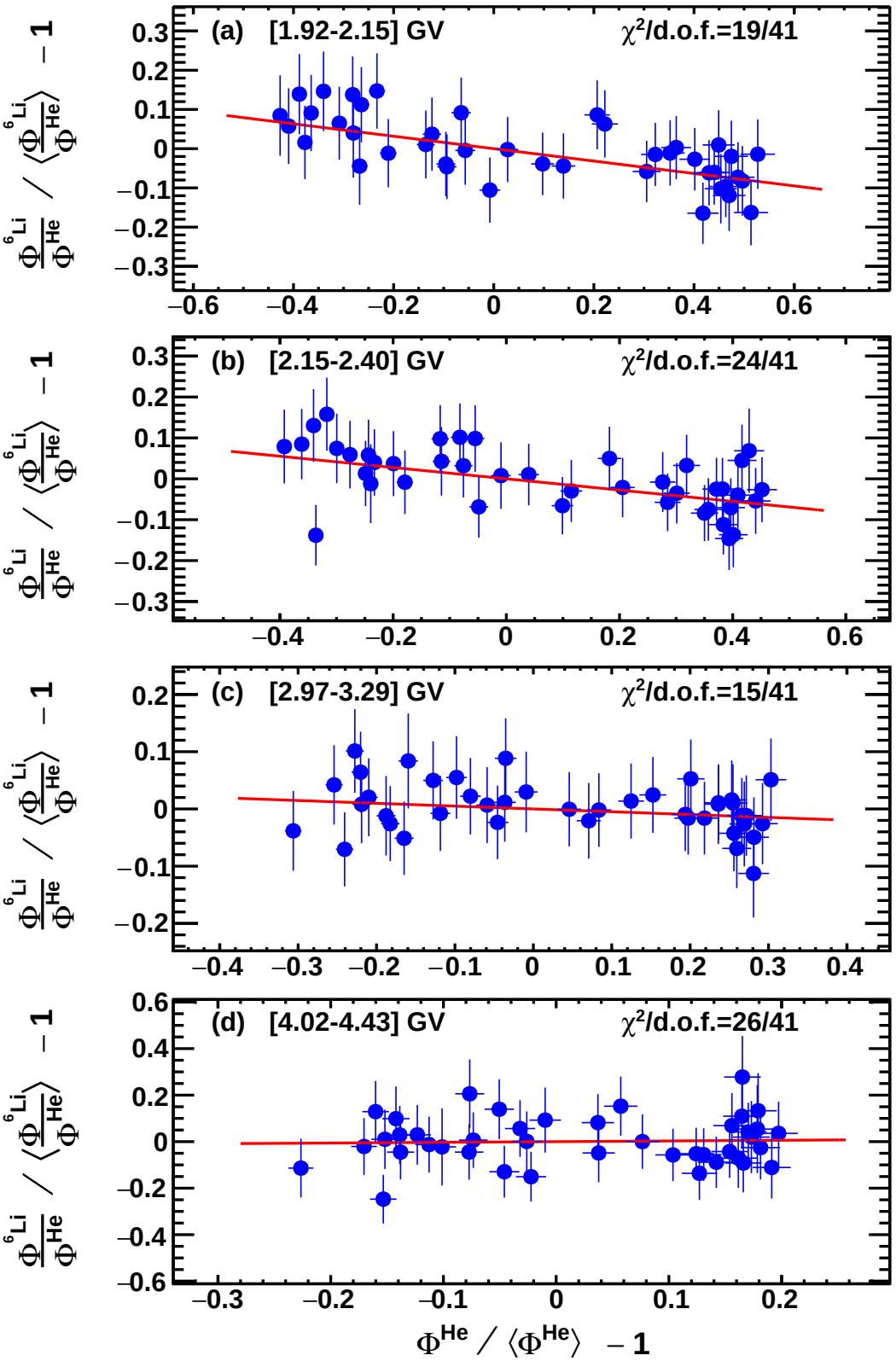

FIG. S10. The relative variation of $\Phi^{^6\mathrm{Li}}/\Phi^{\mathrm{He}}$ as a function of the relative variation of Φ^{He} for (a) [1.92-2.15] GV, (b) [2.15-2.40] GV, (c) [2.97-3.29] GV, and (d) [4.02-4.43] GV. The red lines show fit results with Eq. (2) to obtain the slope $k^{^6\mathrm{Li}}$. The χ^2/d.o.f. of the fits are also shown in the figure.

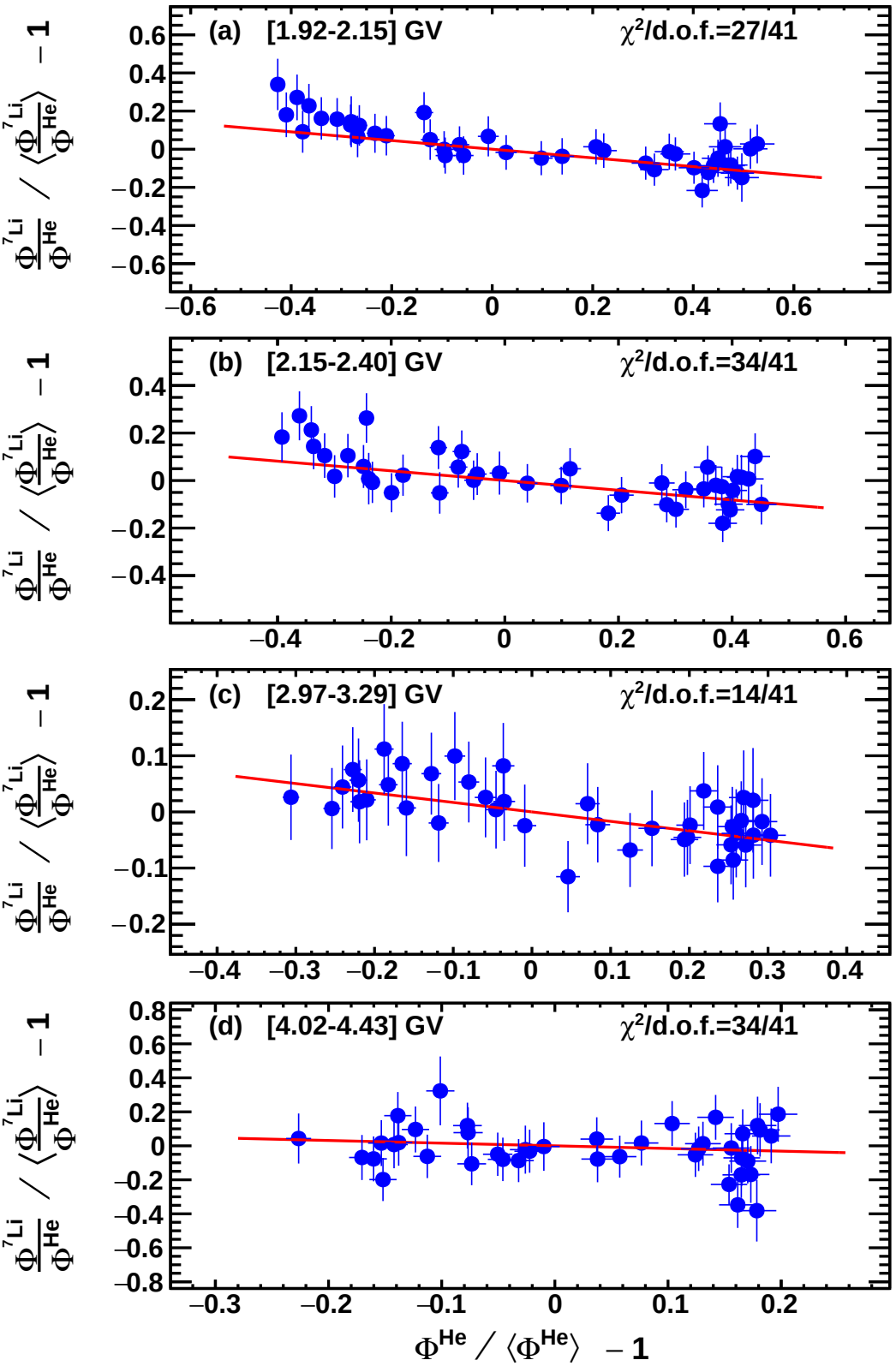

FIG. S11. The relative variation of $\Phi^{^7\mathrm{Li}}/\Phi^{\mathrm{He}}$ as a function of the relative variation of Φ^{He} for (a) [1.92-2.15] GV, (b) [2.15-2.40] GV, (c) [2.97-3.29] GV, and (d) [4.02-4.43] GV. The red lines show fit results with Eq. (3) to obtain the slope $k^{^7\mathrm{Li}}$. The χ^2/d.o.f. of the fits are also shown in the figure.

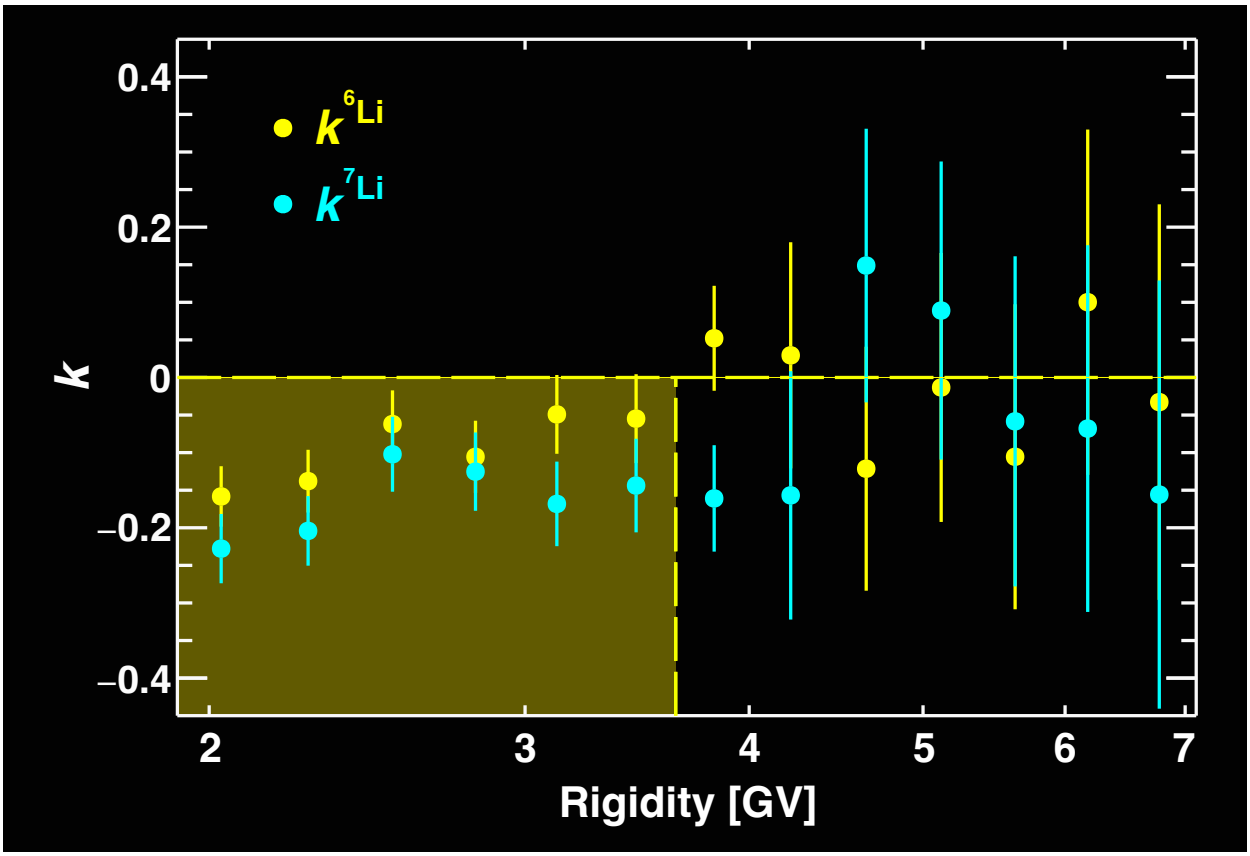

FIG. S12. Fitted $k^{^6\mathrm{Li}}$ and $k^{^7\mathrm{Li}}$ with Eq. (2) and Eq. (3) as functions of rigidity. As seen, both $k^{^6\mathrm{Li}}$ and $k^{^7\mathrm{Li}}$ are below zero from 1.9 to 3.64 GV (shaded region), showing that the $\Phi^{^6\mathrm{Li}}$ and $\Phi^{^7\mathrm{Li}}$ are less modulated than the Φ^{He} in this rigidity range. $k^{^6\mathrm{Li}}$ and $k^{^7\mathrm{Li}}$ are compatible with zero above 4.02 GV, showing that the $\Phi^{^6\mathrm{Li}}$, $\Phi^{^7\mathrm{Li}}$, and Φ^{He} exhibit identical variations with time above ∼4 GV.

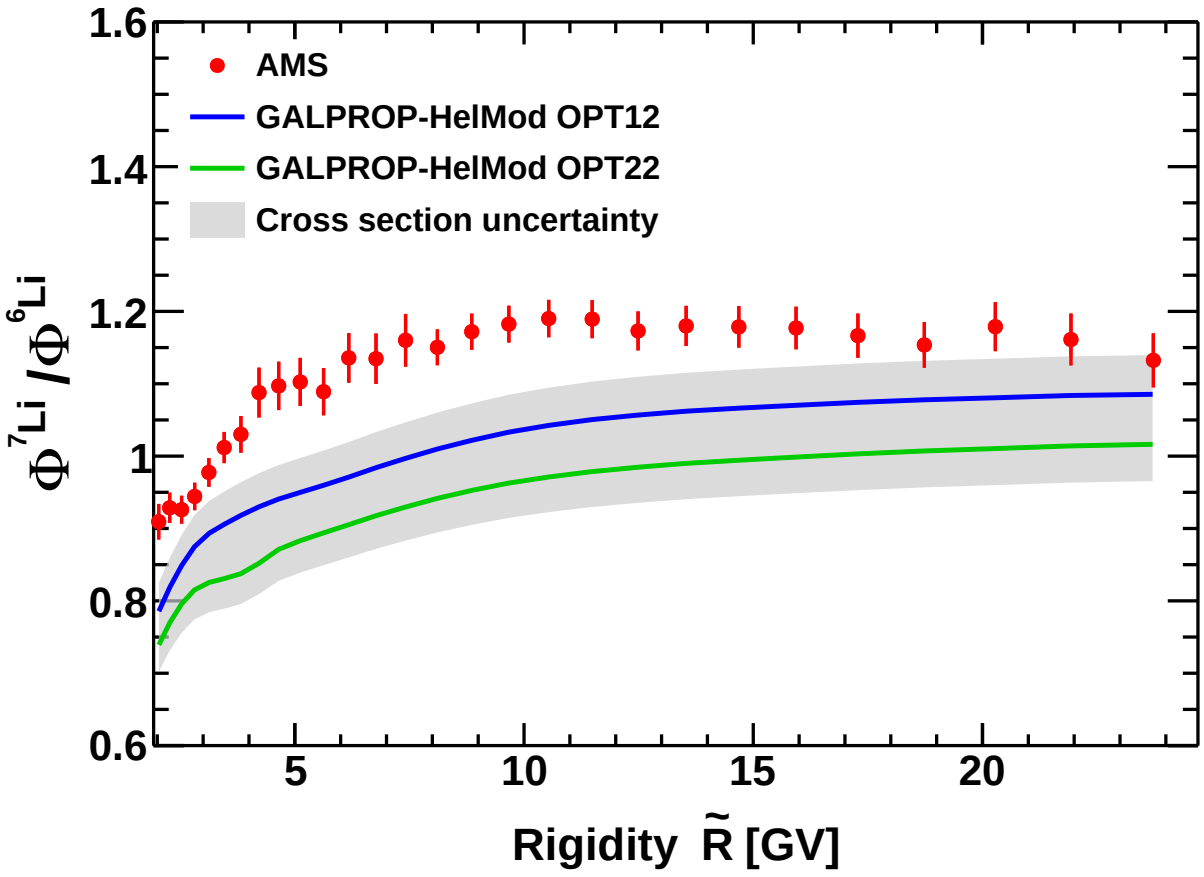

FIG. S13. The AMS $\Phi^{^7\mathrm{Li}}/\Phi^{^6\mathrm{Li}}$ together with the predictions of the latest GALPROP model using two different cross-section parametrizations, OPT12, OPT22, see Ref. [44] for definitions. Only the secondary origin of both Li isotopes is assumed [45]. The gray area represents the conservative estimate of cross section related uncertainties to $\Phi^{^7\mathrm{Li}}/\Phi^{^6\mathrm{Li}}$. It includes the difference between two parametrizations ($\sim$10%) and an additional 5% systematic uncertainty as suggested by the model author [44]. As seen, neither model prediction agrees with the AMS result.

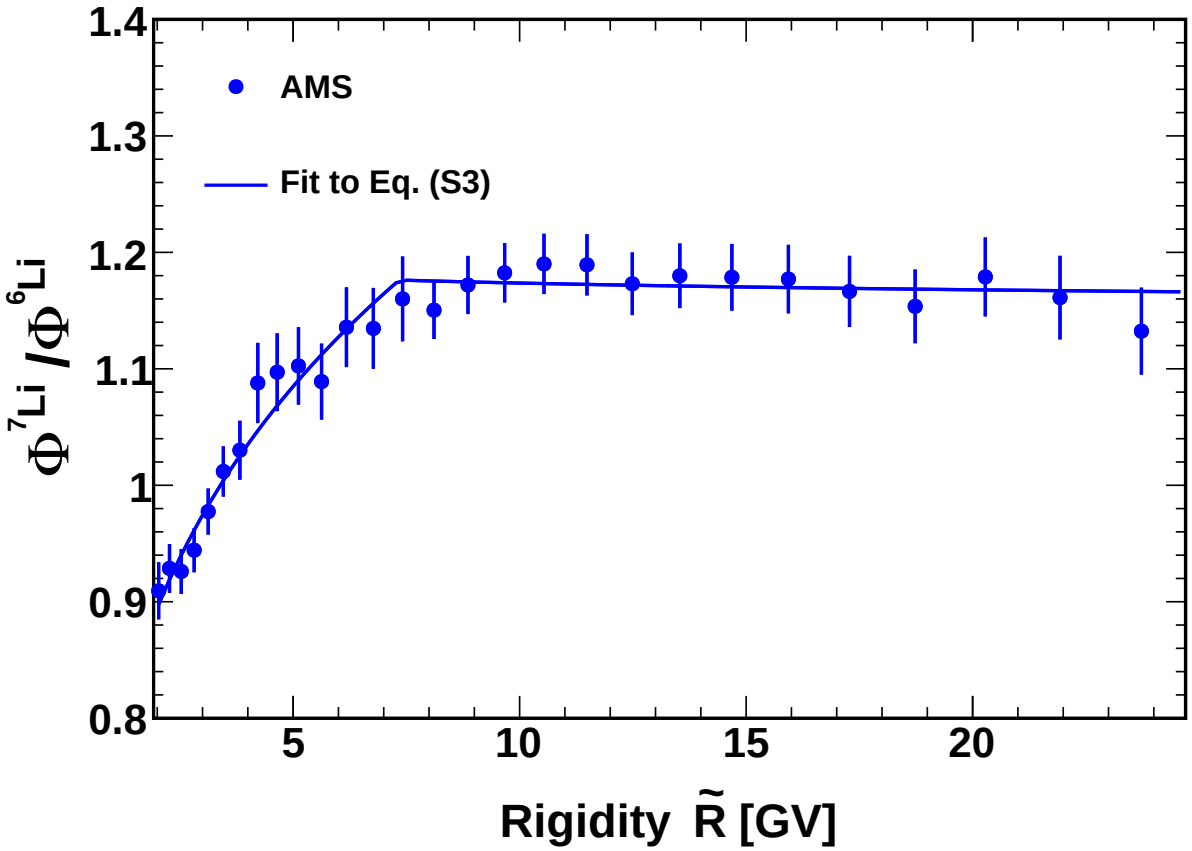

FIG. S14. The AMS time-averaged $\Phi^{^7\mathrm{Li}}/\Phi^{^6\mathrm{Li}}$ with total errors as a function of rigidity. The solid blue curve shows the fit result with Eq. (S3). The fit yields $K = 1.17 \pm 0.02$, $R_0 = 7.2 \pm 0.4$ GV, $\Delta_1 = 0.21 \pm 0.01$, and $\Delta_2 = -0.002 \pm 0.011$ with a χ^2/d.o.f. of 23.8/24. The value of Δ_2 is consistent with zero, which confirms that the $\Phi^{^6\mathrm{Li}}$ and $\Phi^{^7\mathrm{Li}}$ have an identical rigidity dependence above $R_0 \sim$7 GV.

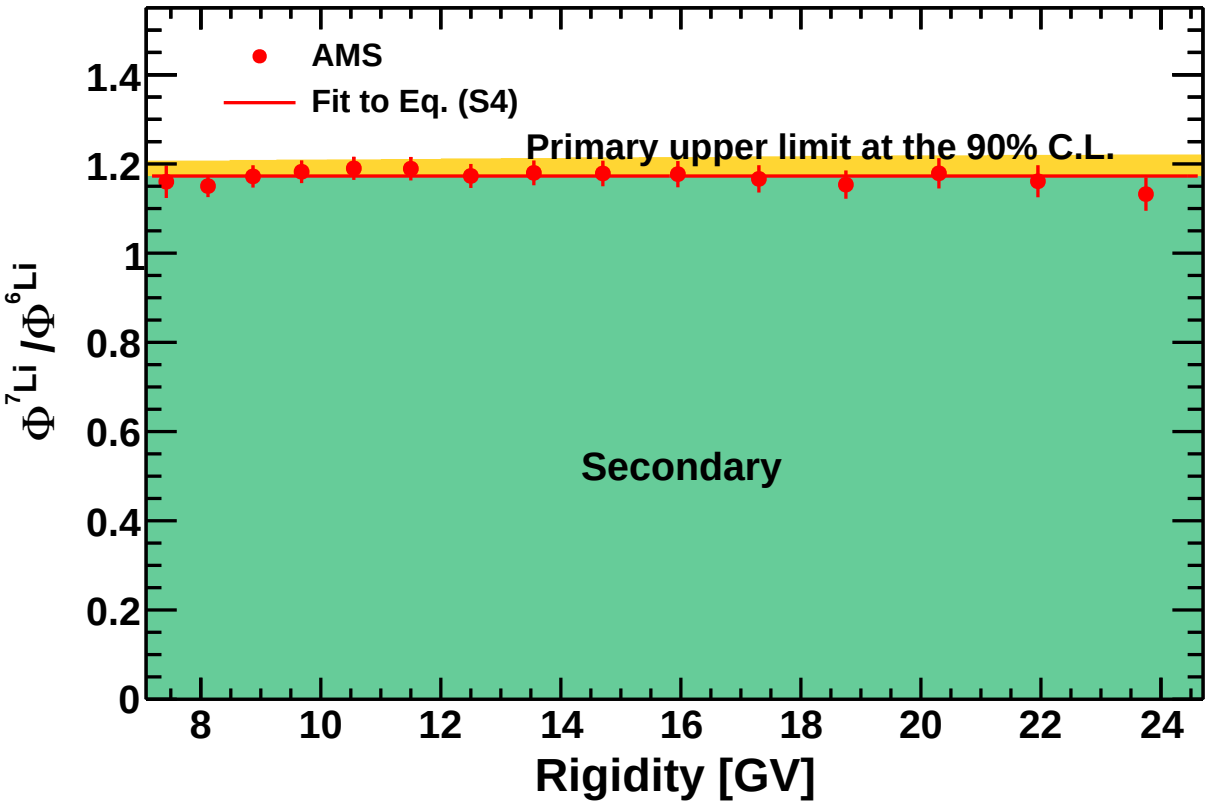

FIG. S15. The AMS time-averaged $\Phi^{^7\mathrm{Li}}/\Phi^{^6\mathrm{Li}}$ with total errors as a function of rigidity. The solid red curve shows the fit result with Eq. (S4). The contribution of the secondary component is indicated by the green shading. The upper limit <3% of the primary component at the 90% C.L. is indicated by the yellow shading.